Journal of Power Sources 196 (2011) 7058–7069

Contents lists available at ScienceDirect

Journal of Power Sources

journal homepage: www.elsevier.com/locate/jpowsour

Design of experiment approach applied to reducing and oxidizing tolerance of anode supported solid oxide fuel cell. Part I: Microstructure optimization

Antonin Faes[a,b,*], Jean-Marie Fuerbringer[b], Driss Mohamedi[c], Aïcha Hessler-Wyser[a], Gilles Caboche[c], Jan Van herle[b]

[a] Interdisciplinary Centre for Electron Microscopy (CIME), Ecole Polytechnique Fédérale de Lausanne (EPFL), CH-1015 Lausanne, Switzerland
[b] Industrial Energy Systems Laboratory (LENI), EPFL, CH-1015 Lausanne, Switzerland
[c] Laboratoire Interdisciplinaire Carnot de Bourgogne, ICB-UMR 5209, CNRS-Université de Bourgogne, 9 Avenue Alain Savary, PB 47870, F-21078 Dijon, France

ARTICLE INFO

Article history:
Received 24 June 2010
Received in revised form 29 July 2010
Accepted 30 July 2010
Available online 6 August 2010

Keywords:
RedOx stability
Ni–YSZ anode supported cell
Solid oxide fuel cell
Design of experiment
Surface response methodology
Conductivity

ABSTRACT

The main drawback of Ni/YSZ anode supports for solid oxide fuel cell application is their low tolerance to reducing and oxidizing (RedOx) atmosphere changes, owing to the Ni/NiO volume variation. This work describes a structured approach based on design of experiments for optimizing the microstructure for RedOx stability enhancement. A full factorial hypercube design and the response surface methodology are applied with the variables and their variation range defined as: (1) NiO proportion (40–60 wt% of the ceramic powders), (2) pore-former proportion (0–30 wt% corresponding to 0–64 vol.%), (3) NiO particle size (0.5–8 μm) and (4) 8YSZ particle size (0.6–9 μm).

To obtain quadratic response models, 25 different compositions were prepared forming a central composite design. The measured responses are (i) shrinkage during firing, (ii) surface quality, (iii) as-sintered porosity, (iv) electrical conductivity after reduction and (v) expansion after re-oxidation. This approach quantifies the effect of all factors and their interactions. From the quadratic models, optimal compositions for high surface quality, electrical conductivity (>500 S cm^{-1} at room temperature) and RedOx expansion (<0.2% upon re-oxidation) are defined. Results show that expansion after re-oxidation is directly influenced by the sample porosity whereas, surprisingly, the NiO content, varied between 40 and 60 wt%, does not show any impact on this response.

1. Introduction

As energy demand is increasing, more efficient systems and sustainable technology are required. Solid oxide fuel cells (SOFCs) can reach high efficiency even for small systems and are able to use a large variety of fuels (hydrogen, natural gas, biogas, etc.) [1]. Used as electrolyzer, they can store excess energy production from renewable intermittent sources such as photovoltaics, hydro-, wind- and tide-turbines.

State-of-the-art intermediate temperature (650–850 °C) SOFC technology is based on a thin yttria-stabilized zirconia (YSZ) electrolyte supported by a nickel–YSZ cermet anode. The main drawback of this design is its sensitivity to nickel re-oxidation (known as "RedOx" cycling). Oxidation of the nickel is accompanied by a volume increase of 71% [2]. If the anode support and/or the anode active functional layer (AFL) expand more than 0.2%, the induced tensile stresses will provoke cracks in the thin electrolyte [2–4]. The re-oxidation can occur (i) at high current density or high fuel utilization, (ii) near compressive seals [5], (iii) due to fuel starvation and (iv) due to fuel saving during startup and cool-down of the system. The RedOx stability of the cells is especially important for small systems (1–5 kW) where a safety/emergency gas add-on is not economically feasible.

Changes in the anode microstructure have an influence on the RedOx behavior. Waldbillig et al. observed that the expansion upon RedOx cycling decreased for a coarse microstructure compared to a fine one whereas the NiO content did not show a major influence [6]. The coarse microstructure enhances the RedOx stability. In a similar way, Pihlatie et al. showed that high porosity samples lower the expansion during RedOx cycles [7]. The use of a cermet containing 3 mol% YSZ showed better RedOx stability due to the higher strength of 3YSZ compared to 8YSZ [3].

Microstructure optimization of anodes has been looked at since a while in the SOFC community [8]. These optimizations were applied initially to increase performance by enhancement of the electrical conductivity, the porosity and triple phase boundary density [9,10]. Later the focus was on durability, like nickel phase coarsening problems [11,12].

* Corresponding author at: Laboratory of Industrial Energy Systems (LENI), Ecole Polytechnique Fédérale de Lausanne (EPFL), Station 9, CH-1015 Lausanne, Switzerland. Tel.: +41 21 693 6813; fax: +41 21 693 3502.
E-mail address: antonin.faes@epfl.ch (A. Faes).

0378-7753/$ – see front matter © 2010 Elsevier B.V. All rights reserved.
doi:10.1016/j.jpowsour.2010.07.092

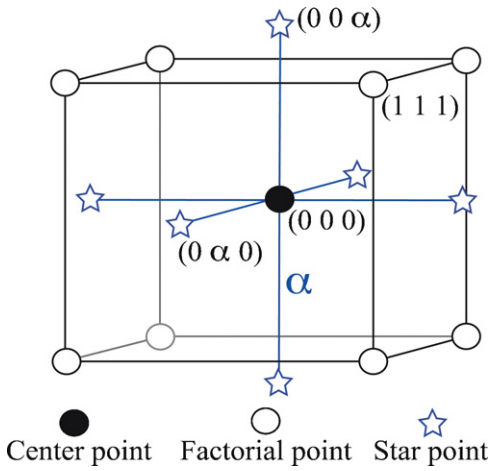

Fig. 1. Central composite design for three factors ($k = 3$).

A statistical approach for optimization of a complex system can reduce the number of experiments compared to the traditional trial and error method. This approach is known as design of experiment (DoE) and response surface methodology (RSM), from the work of R.A. Fisher in the first quarter of the last century [13,14]. This mathematical method gives a model that links the processing conditions or the composition of a product (called factors) with the properties of this product (measured responses). From this model, optimal processes and mixtures can be obtained using a reduced number of experiments [15,16]. The approach was already applied to SOFC anode fabrication for plasma spray [17] and uniaxial compaction methods [18]. The procedure can also be used to assess the main factors responsible for long term degradation [19].

The goal of this study is to find an optimal anode support microstructure in particular with respect to re-oxidation resistance. The desired responses of the support are (i) an expansion lower than 0.2% after a RedOx cycle, (ii) sufficient electrical conductivity in reduced state (>500 S cm^{-1} at room temperature) and (iii) good sinterability (no cracks or surface defects after sintering). The composition of the prepared samples was varied using different factors: (1) the NiO content in the ceramic phase, (2) the pore-former content, (3) the NiO particle size and (4) the YSZ particle size.

2. Design of experiment

2.1. Factorial design and response surface

The idea of factorial design is to observe the effects of the factors and their interaction on the measured responses with relatively fewer experiments. Factors can be quantitative (e.g. concentration) or qualitative (e.g. different catalysts or different powder types). The simplest design uses only two levels of each factor, basically the minimum and the maximum, which are noted in coded value −1 and +1, respectively, for simplification. For full factorial design all the possible combinations are executed, but when the factors are numerous, fractional factorial design can be used [15,16].

The central composite design (CCD) is widely used for response surface methodology (RSM) for a second-order model [15,16]. This design involves two overlapping designs: a two level factorial design represented by the open symbols in Fig. 1 and an axial or star design represented by the stars in Fig. 1. The factorial points represent the variance-optimal design for a first order plus two-factor interaction model. The center point and star points allow efficient estimation of the quadratic terms (see [16], p. 297). With α, the distance of the star points from the center point, equal to 1, the star points are placed in the center of the cubic faces (or of a hypercube for $k > 3$, where k is the number of factors) and the levels of the factors are defined as −1, 0, +1 (for the minimal, the intermediate and the maximal values of the factor).

Response surface methodology requires a model for the true response surface approximation. If no physical model is known, multiple regressions can be used to build an empirical model. The commonly used technique is the least squares regression model:

$$\mathbf{y} = \boldsymbol{X}\mathbf{a} + \boldsymbol{\varepsilon} \tag{1}$$

where $\mathbf{y}$ is the vector of the n_o observations, $\mathbf{a}$ is the vector of the n_p regression coefficients parameters, $\boldsymbol{X}$ is the $n_o \times n_p$ *model matrix* built from the design of experiment and $\boldsymbol{\varepsilon}$ is the vector of random errors. The *model matrix* (based on −1 and +1) will be converted into the *experimental matrix* when the range of the factors is defined (see next section and Table 1). The unbiased least squares estimator of $\mathbf{a}$ is given by

$$\mathbf{a} = (\boldsymbol{X}'\boldsymbol{X})^{-1}\boldsymbol{X}'\mathbf{a} \tag{2}$$

where $\boldsymbol{X}'$ is the transposed model matrix, $(\boldsymbol{X}'\boldsymbol{X})^{-1}$ is the *dispersion matrix*. The built model is then given by

$$Y(x) = a_0 + \sum_{i=1}^{4} a_i x_i + \sum_{j=1}^{4}\sum_{i=1}^{4} a_{ij} x_i x_j + \varepsilon(0, \sigma^2) \tag{3}$$

with $Y(x)$ an estimation of the measured response $\boldsymbol{y}$, a_0 the constant effect, a_i the main half-effects of factors x_i, $a_{ij,(i \neq j)}$ the first order interaction half-effects, a_{ii} the quadratic half-effects and $\varepsilon(0,\sigma^2)$ the residuals that should follow a Gaussian distribution centered on zero ($E(\varepsilon) = 0$) with a variance of σ^2 ($\mathrm{Var}(\varepsilon) = \sigma^2$).

The comparison between different models of the same response (i.e. linear model versus quadratic model) can be made using the adjusted coefficient of linear regression, R^2_{adj}, as the standard coefficient of linear regression, R^2, will always improve when parameters are added to the model:

$$R^2 = 1 - \frac{SS_E}{SS_T} \tag{4}$$

$$R^2_{adj} = 1 - \frac{n_o - 1}{n_o - n_p}(1 - R^2) \tag{5}$$

where SS_T is the sum of squares of the observations, and SS_E is the sum of squares of the errors or residuals (the residual i is the difference between observation, y_i and the fitted value, Y_i), n_o is the number of observations and n_p is the number of parameters used in the model.

2.2. Experimental factors and measured response

The factors are the studied experimental variables that could influence the sample properties (also noted as measured responses of the sample). The experimental factors in this study are: (1) the NiO weight fraction in the ceramic phase, (2) the pore-former content added to the ceramic powders, (3) the NiO particle size and (4) the 8YSZ particle size. All the natural and coded values are summarized in Table 1. The natural value is the chosen interval for the factor (e.g. 0, 15 and 30 wt% of pore-former) and the corresponding coded (or standardized) variables change from −1 to +1 on the full interval. The use of the coded values is for the ease of the matrix calculus.

2.2.1. Weight fraction of NiO

The weight fraction of NiO is calculated only for the ceramic phase (i.e. excluding pore-former). The natural variable for NiO weight fraction ($u_{1,\mathrm{NiO}}$) is obtained as follows:

$$u_{1,\mathrm{NiO}} = \frac{m_{\mathrm{NiO}}}{m_{\mathrm{NiO}} + m_{\mathrm{YSZ}}} \times 100 \tag{6}$$

Table 1
Variables or factors studied: from natural to coded values.

	Factors\coded value x_i	−1	0	1
u_1	NiO/YSZ fraction	40/60 wt%	50/50 wt%	60/40 wt%
u_2	Pore-former fraction	0 wt%	15 wt%	30 wt%
u_3	NiO particle size	Fine	50 wt% fine/50 wt% coarse	Coarse
u_4	8YSZ particle size	Fine	50 wt% fine/50 wt% coarse	Coarse

with $40 \le u_{1,\mathrm{NiO}} \le 60$, m_{NiO} and m_{YSZ} the mass of NiO and YSZ, respectively.

The standardized variable for NiO weight fraction ($x_{1,\mathrm{NiO}}$) is

$$x_{1,\mathrm{NiO}} = \frac{u_{1,\mathrm{NiO}} - u_{1,\mathrm{NiO}}(0)}{\Delta u} \tag{7}$$

with $u_{1,\mathrm{NiO}}(0)$ the center of the natural interval and Δu half of the natural interval. Then the interval for the natural variable $u_{1,\mathrm{NiO}} = [40,60]$ corresponds to the interval for the standardized variable $x_{1,\mathrm{NiO}} = [-1,1]$. This is done for all the measured variables.

The natural variable for YSZ weight fraction ($u_{1,\mathrm{YSZ}}$) is

$$u_{1,\mathrm{YSZ}} = 100 - u_{1,\mathrm{NiO}} \tag{8}$$

2.2.2. Pore-former (PF) fraction

The weight proportion of pore-former (u_2) is added to the total weight of ceramics (NiO + YSZ):

$$u_2 = \frac{m_{Pore-former}}{m_{\mathrm{NiO}} + m_{\mathrm{YSZ}} + m_{Pore-former}} \times 100 \quad \text{with } 0 \le u_2 \le 30 \tag{9}$$

Using equations in Appendix B and densities in Table B1 and 1.55 g cm^{-3} for the pore-former (PF), 15 wt% PF corresponds to 41–42 vol.% PF, depending of the weight fraction of NiO and 30 wt% PF corresponds to 63–64 vol.% PF.

2.2.3. NiO and 8YSZ particle size

Two different types of nickel oxide and 8YSZ were used here. The powder characterization will be described later. The standardized variable for NiO size is given by

$$x_3 = 2\frac{m_{coarse}}{m_{fine} + m_{coarse}} - 1 \tag{10}$$

The standardized variable for the 8YSZ particle size is calculated in the same way.

The measured responses are the following:

- Shrinkage after firing 4 h at 1400 °C in air.
- Qualitative observation of the sample surface after sintering.
- Porosity in as-sintered and reduced state.
- Conductivity at room temperature after reduction for 24 h at 800 ± 5 °C in a flow of 8% H_2 in N_2.
- Expansion at room temperature after re-oxidation during 24 h at 845 ± 5 °C in air.

3. Experimental

3.1. Raw powder characterization

Different powders were used for this study, two NiO and two 8YSZ (8 mol% Y_2O_3–ZrO_2) powders, and an organic pore-former. Particle size measurements were carried out by laser diffraction and specific surface area determination. The pore-former was also studied by thermogravimetric analysis (TGA).

Particle size distributions were obtained by laser diffraction using a Mastersizer (Malvern Inst. (UK)), with Mastersize S 2.15 software. The analysis model is polydisperse and the refractive index of the solvent is 1.33. The analysis was done in an aqueous suspension with 0.02% PAA (poly acrylic acid) dispersant after 15 min of applying the ultrasound horn. The refractive indexes used for the powders are 2.37, 2.10 and 1.52 for NiO, YSZ and pore-former, respectively and the densities are 1.55 g cm^{-3} for the pore-former and summarized in Table B1 for NiO and YSZ [20,21].

Specific surface area measurements were carried out with a Micrometrics Gemini® 2376 instrument using a classical 5 point-measurement. Prior to the measurement, the samples were heated 1 h at 200 °C under a nitrogen flux to remove any adsorbed water.

Thermogravimetric analysis was performed with a TGA SDTA851 instrument from Mettler Toledo® at a ramp rate of 2 °C min^{-1} from room temperature up to 800 °C under air flow in a 150 μl alumina crucible.

3.2. Sample preparation and microstructure comparison

Planar SOFC anode supports are usually fabricated by tape casting, a well-known technique easy to upscale [22,23]. The technique uses slurries dispersed by a wet ball-milling process with an optimized composition of solvent, dispersant, binder, plasticizer and defoamer. As this study is focused on the powder size, pore-former and the phase proportions of the samples, and not on the optimization of the wet slurry, a dry ball-milling process was used, with Turbula® equipment followed by an isostatic compaction in cylinder shape.

The duration of dry ball-milling, with 0.5 wt% of stearic acid as dispersant, was optimized to obtain the same microstructure than after standard wet ball-milling during 24 h. The microstructure after 2, 4, 6, 8 and 10 h of dry ball-milling was compared to standard samples (obtained from 24 h wet ball-milling) by using a scanning electron microscope (FEI Xlf-30 SFEG Sirion, at 10 kV, with backscattered electrons (BSE) detector, spot size 4, working distance 5 mm and a magnification of 1500×) after polishing the NiO–YSZ samples down to 0.5 μm with diamond lapping film and water as lubricant and cooling medium. From these observations, 8 h of dry milling in a Turbula® mill appeared to yield a microstructure closest to the standard one. For shorter times, agglomerates remained, whereas for longer times, the microstructure became finer due to further particle size reduction of the powders. Therefore, the dry ball-milling process for the tested samples was fixed at 8 h in the Turbula® mill with 0.5 wt% of stearic acid (relative to total powder mass) and 1 more hour with 1 wt% of Duramax® B1000 acrylic binder (relative to total mass).

To obtain homogeneous microstructures in a compacted sample, the mixed powder was isostatically pressed at 200 MPa for 1 min (ramp of 1 kN s^{-1} and plateau at 400 kN) in a silicone cylinder of 10 mm diameter and 40 mm length. Sample faces were polished parallel with 600 mesh SiC paper, for their length measurement done with a micrometer.

Sintering was done for 4 h in air at 1400 °C, with a 1 °C min^{-1} ramp from room temperature to 800 °C and a 3 °C min^{-1} ramp from 800 to 1400 °C. Cooling occurred with a 1 °C min^{-1} ramp from 1400 to 1100 °C and then naturally down to room temperature.

Reduction was carried out in a tubular furnace. The procedure was to first heat at 10 °C min^{-1} up to 800 °C ± 5 °C under an air flux of 1 l min^{-1}. After 1.5 h of temperature stabilization, nitrogen was introduced for 20 min at 1.8 l min^{-1} for a purge. Then 8% H_2 in

Table 2
Measurements taken on the cylindrical samples at the different stages.

	Before sintering	After sintering	After reduction	After re-oxidation
Mass [g] ± 0.001 g	√	√	√	√
Length [mm] ± 0.001 mm	√	√	√	√
Diameter [mm] (two measurements at the extremities and two at the center) ± 0.01 mm		√		
Conductivity (S cm^{-1})			√	

Table 3
Powder characterizations.

Powders	Light diffraction, d_{v50} (μm) (span)	Specific surface area, S_{BET} (m^2 g^{-1})	d_{BET} (μm)	Factor of agglomeration d_{v50}/d_{BET}
NiO fine	0.52 (2.88)	4.29	0.209	2.5
NiO coarse	8.37 (2.25)	2.79	0.322	26.0
8YSZ fine	0.57 (3.45)	10.98	0.090	6.3
8YSZ coarse	9.08 (1.07)	0.66	1.502	6.0
Pore-former	8.56 (1.61)	0.78	4.962	1.7

N_2 (form gas) was flown at 1–1.5 l min^{-1} for 24 h, and finally the furnace cooled down at 10 °C min^{-1} under form gas.

A similar procedure was applied for oxidation, switching gas appropriately. The plateau was fixed at 845 ± 5 °C. This error was due to the temperature distribution inside the tubular furnace. Temperature increased when starting the air flow, due to the strong exothermicity of nickel oxidation. During the experimental procedures, sample fabrication was reproduced from 1 to 4 times.

3.3. Sample measurements

Measurements taken on the cylindrical samples at the different stages are listed in Table 2. As no variation of length was measured between as-sintered and reduced state, the shrinkage of the sample during reduction is neglected.

Porosity proportion (p_{pore}) of the sample was extracted directly from the measured mass (m_{sample}) and volume of the sample (V_{sample}).

$$p_{pore} = \frac{V_{pore}}{V_{sample}} = 1 - \frac{1}{\rho_{th}} \frac{m_{sample}}{V_{sample}} \quad (11)$$

with ρ_{th} density of the composite materials (known from the composition).

Conductivity (σ) in S cm^{-1} of a sample is obtained by measuring the potential drop (ΔV) in V between two contacts separated by a known distance (d) in cm:

$$\sigma\,[\mathrm{S\,cm^{-1}}] = \frac{d \cdot I}{\pi r^2 \cdot \Delta V} \quad (12)$$

with r the radius in cm of the sample and I a constant current in A passed through the sample (4-point method).

4. Results and discussion

4.1. Powder characterizations

A summary of the powder characterizations is given in Table 3 The d_{v50} is the equivalent volume spherical diameter at which half of the particles volume is bigger and half is smaller than this value [24]. The span gives a measure of the particle size distribution and is given by

$$\mathrm{Span} = \frac{d_{v90} - d_{v10}}{d_{v50}} \quad (13)$$

where d_{v10} and d_{v90} are particle sizes where 10 and 90 vol.% are smaller than this value, respectively.

From the specific surface measurement (S_{BET}), a monodisperse spherical diameter (d_{BET}) can be calculated:

$$d_{BET}[\mu\mathrm{m}] = \frac{6}{S_{BET}[\mathrm{m^2\,g^{-1}}] \cdot \rho[\mathrm{g\,cm^{-3}}]} \quad (14)$$

where ρ is the powder density.

The light scattering results show that the fine powders have a diameter of about half a micron and that the coarse powders and the pore-former have a diameter around 9 μm. But if we compare the specific surface area measurements, the coarse NiO shows agglomerations that are not broken down during the ultrasound treatment before light scattering measurements. These agglomerates are also observed in Fig. 2b. The energy of the ball-milling treatment is higher than the one from the ultrasound treatment, so agglomerates can break during the homogenizing with ball-milling. Fig. 2 shows scanning electron micrographs of the different powders.

Fig. 3 shows the TGA measurement of the pore-former. The first decrease to 90 wt% is due to the evaporation of the water included in the pore-former. It is followed by a stronger decrease around 300 °C corresponding to the release of the chemically bonded water. The ultimate mass variation from 350 to 600 °C comes from the decomposition of the organic phase.

4.2. Raw results

As some sample compositions were replicated the total number of samples is 46 from 25 different compositions (at least one sample of each composition was tested). The central point was repeated three times. The full list of the 25 different compositions and the raw results are presented in supplementary on-line data.

4.2.1. Expansion after re-oxidation

The results show a certain reproducibility depending on the composition of the sample. The main goal of this study being to obtain samples with an expansion after a RedOx cycle lower than 0.2%, one sees that samples from compositions 1, 3, 9, 11 and 20 fulfill this condition. It is interesting to note that all these samples contain only coarse YSZ powder.

The sample surface can be without any apparent defects (surface quality, SQ = 3), show some holes and small cracks (SQ = 2) or larger cracks (SQ = 1) (see Fig. 4a–c). The low expansion samples are all poor in surface quality as shown by Fig. 4d. Only the composition 3 could give an intermediate SQ value. A low SQ value will not be appropriate from a fabrication point of view.

Expansion after re-oxidation is strongly influenced by the porosity of the samples as shown in Fig. 5. With as-sintered porosity lower than 35 vol.%, it is not possible to achieve the 0.2% expansion limit. However, also several samples with porosity above 45 vol.%

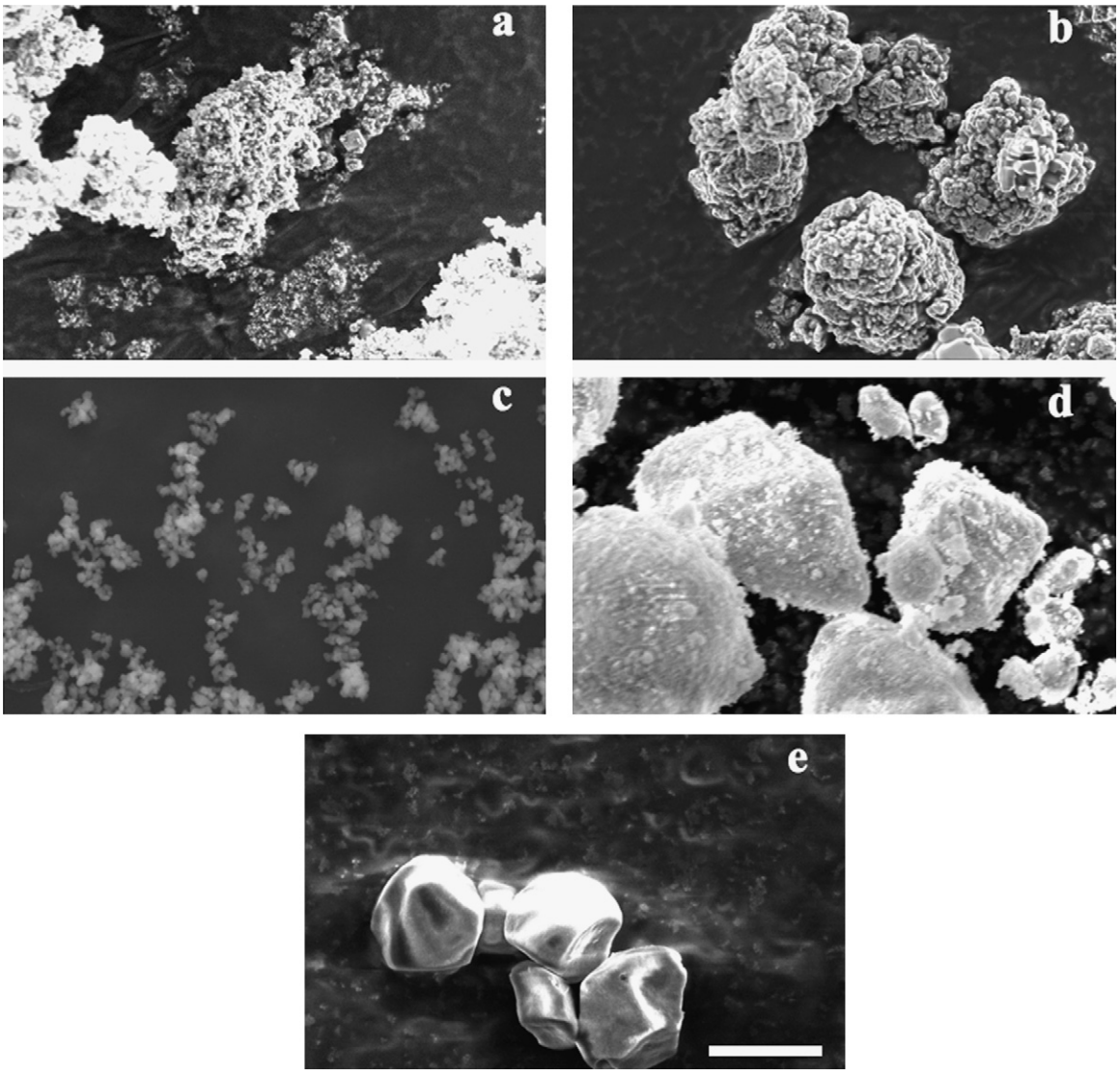

Fig. 2. Scanning electron micrographs of the powders: (a) NiO fine, (b) NiO coarse, (c) 8YSZ fine, (d) 8YSZ coarse and (e) pore-former (marker length = 5 μm for all micrographs).

showed a slightly too high expansion. The relation between expansion after re-oxidation (e) and the as-sintered porosity (p_{pore}) could be approximated with an exponential or power law:

$$\varepsilon_{\text{exp}} = 8.825 \exp(-0.081 \cdot p_{pore}) \quad (15)$$

$$\varepsilon_{pow} = 697.34(p_{pore})^{-2.044} \quad (16)$$

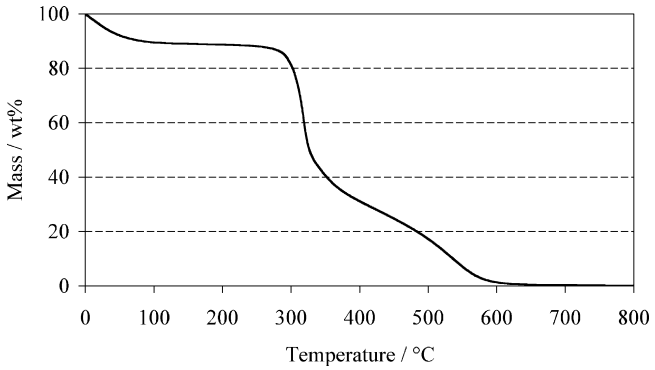

Fig. 3. Mass variation of the pore-former with temperature.

The R^2 coefficient was slightly better for the exponential fit ($R^2_{\text{exp}} = 0.725$) compared to the one from the power law ($R^2_{\text{pow}} = 0.693$). The 0.2% RedOx expansion limit corresponded to 47 and 54% porosity proportion for exponential and power law approximations, respectively. In other words, a NiO–YSZ anode support needs a porosity after sintering around 50% to be RedOx stable.

Pihlatie et al. showed that changing the porosity of a sample from 9 to 33% by reducing the temperature of firing by 20 K and introducing pre-calcined NiO powder, the cumulative RedOx strain was decreased by a factor of 20 [7]. If we introduce these porosity values into Eqs. (15) and (16), the resulting factor decrease in linear expansion is calculated to be equal to 7 and 14, respectively. The trend in the present study is thus quite similar compared to the findings of Pihlatie et al. [7].

4.2.2. Porosity after reduction

For convenience, the composition of a cermet is prepared in weight percentage (wt%), w_i. Conductivity calculation is related to the volume percentage (vol.%) of the conducting phase in the solid (v_{Ni}) as well as the porosity fraction (p_{pore}). The weight and the volume fractions in the cermet change during the chemical reaction of reduction or oxidation due to the variation of molar mass and molar volume. The molar percentage (mol%), n_i, of Ni as NiO or Ni

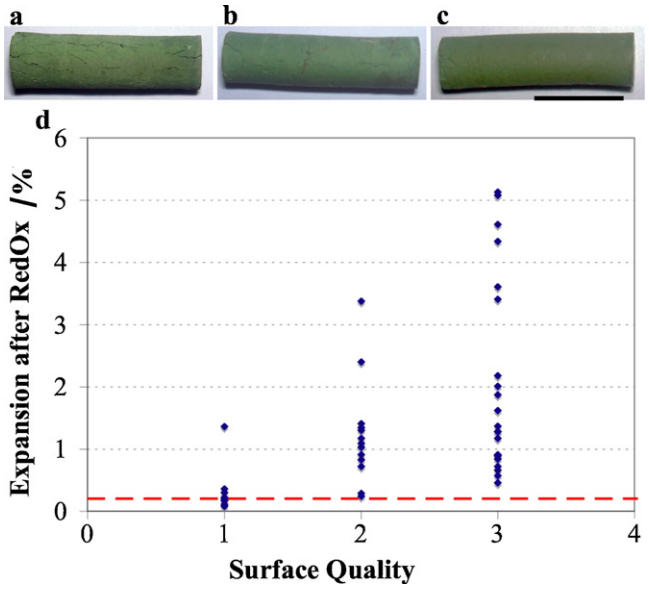

Fig. 4. Example of the different surface qualities (SQ): (a) SQ = 1 (composition 3), (b) SQ = 2 (composition 21), (c) SQ = 3 (composition 16), and (d) expansion after re-oxidation versus SQ (the dashed line is the RedOx limit). Marker length = 1 cm.

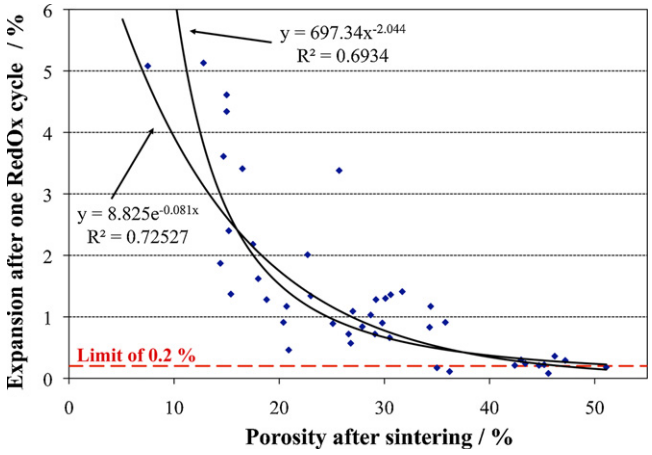

Fig. 5. Expansion after re-oxidation at 845 °C versus as sintered porosity.

stays constant in the cermet. The fraction of the nickel or nickel oxide phase in the composite is given in Table 4 for the different studied samples. The equations and the values used to construct the table are given in Appendix A.

If the volume of the sample is constant during reduction, the porosity variation can be calculated by combining Eqs. (B4), (B11) and (B12). This gives the following relation between the initial porosity after sintering (oxidized state), $p_{pore,ox}$ and the reduced sample porosity, $p_{pore,red}$.

$$p_{pore,red} = \zeta + (1-\zeta)p_{pore,ox} \quad (17)$$

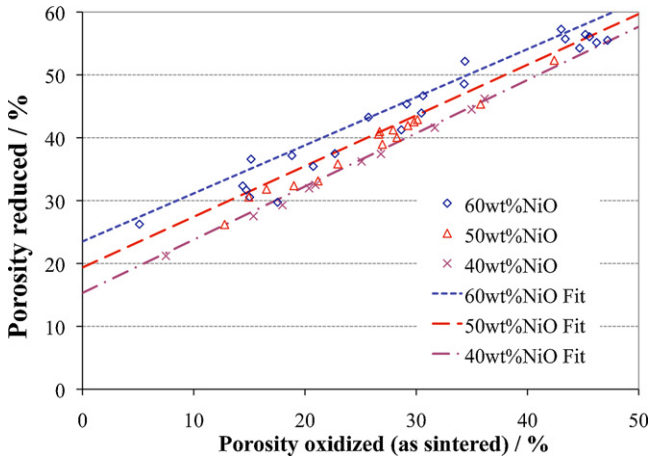

Fig. 6. Oxidized porosity (as sintered) versus reduced porosity (24 h at 800 °C in 8 mol% H_2 in N_2) measurements (diamonds: 60 wt% NiO, triangles: 50 wt% NiO, crosses: 40 wt% NiO) compared to Eq. (17) (lines).

$$\text{with } \zeta = \frac{1-(V_{Ni}/V_{NiO})}{1+((1/w)-1)(\rho_{NiO}/\rho_{YSZ})}$$

where w is the weight fraction of NiO, V_{Ni} and V_{NiO} are the molar volume of nickel and its oxide, respectively, ρ_{NiO} and ρ_{YSZ} are the respective densities. Radovic and Lara-Curzio had a similar approach using a different equation [25].

The measured porosity before and after reduction for 24 h at 800 °C in 8% H_2 in N_2 are compared to equation 17 in Fig. 6. The model is accurate for the 40 wt% NiO measurements, but slightly overestimates the 50 and 60 wt% NiO values. This could be due to the fact that reduction is not completed after 24 h for a cermet with higher nickel content. As the samples are relatively thick (diameter between 5 and 8 mm depending on the sintering shrinkage), the reduction will take a certain time, as the gas has to diffuse in the entire volume. The higher the nickel oxide content, the longer the time needed for complete reduction. The volume fraction of NiO varies from 37 to 57 vol.% NiO, the nickel oxide can agglomerate and forms coarse particles after sintering for high NiO fraction samples.

4.2.3. Electrical conductivity

Conductivity of the sample will depend on the proportion of the different conducting phases as well as on the porosity fraction. The basic conductivity approximation is obtained from the mean value of the conductivities as a function of the phase fractions (model 1):

$$\sigma_{comp,1} = p_{Ni}\sigma_{Ni} + p_{YSZ}\sigma_{YSZ} + p_{pore}\sigma_{pore} \quad (18)$$

where σ_i are the electrical conductivities of the composite and the different phases and p_i are the volume fractions of each phase in the sample ($p_{Ni} + p_{YSZ} + p_{pore} = 1$). The electrical conductivity of Ni and 8YSZ at 25 °C is equal to 146,200 and 0.006 S cm^{-1}, respectively [9,26]. As the conductivity of the pore is assumed equal to zero, the

Table 4
Comparison of the nickel or nickel oxide fraction for the studied sample (w: weight fraction, v: volume fraction in the solid phase, n: mole fraction, p_i: volume fraction including porosity, and ζ, the origin of Eq. (17)).

Weight fraction oxidized: w_{NiO}	40 wt% NiO	50 wt% NiO	60 wt% NiO
Molar fraction: $n_{NiO} = n_{Ni}$	0.533	0.631	0.720
Volume fraction oxidized: v_{NiO}	0.371	0.469	0.570
Volume fraction reduced: v_{Ni}	0.258	0.343	0.439
Weight fraction reduced: w_{NiO}	0.344	0.440	0.541
ζ (reduced porosity for dense oxidized sample, $p_{pore,ox} = 0$)	0.152	0.193	0.234

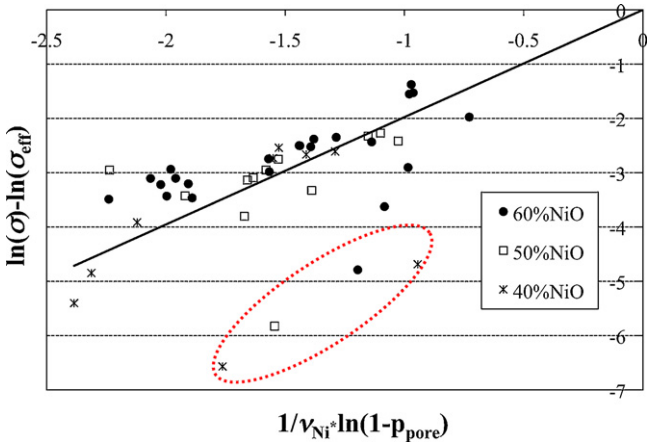

Fig. 7. Linearization of model 3 (Eq. (22)). Measurements in the dashed circle could be due to bad electrical contacts during measurement.

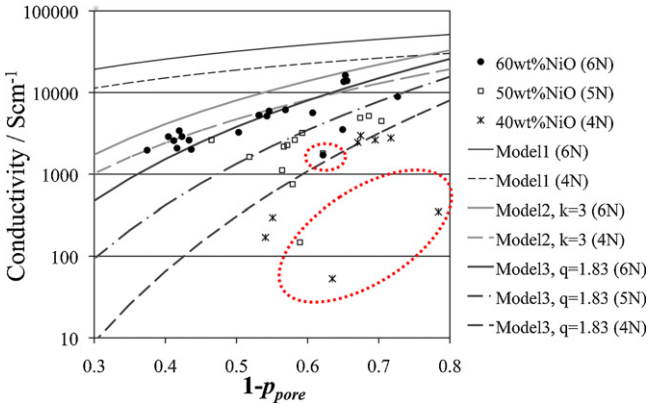

Fig. 8. Conductivity versus the solid fraction ($p_{solid} = 1 - p_{pore}$) and the NiO weight fraction in the ceramic mixture. Measurements in the dashed circle could be due to bad electrical contact during measurement (same measurements than in Fig. 7).

last equation can be rewritten as

$$\sigma_{comp,1} = (1 - p_{pore})\sigma_{eff} \tag{19}$$

with $\sigma_{eff} = \nu_{Ni}\sigma_{Ni} + \nu_{YSZ}\sigma_{YSZ}$

where ν_{Ni} and ν_{YSZ} are the Ni and the YSZ volume fraction in the solid phase ($\nu_{Ni} + \nu_{YSZ} = 1$ and $1 - p_{pore} = p_{Ni}/\nu_{Ni} = p_{YSZ}/\nu_{YSZ}$). A similar model uses an additional power law parameter, k, to fit the conductivity [27] (model 2) to:

$$\sigma_{comp,2} = (1 - p_{pore})^k \sigma_{eff} \tag{20}$$

where k should take a value between 1.5 and 3.

Here, we propose a model including a k value varying with the conducting phase fraction (ν_{Ni}); Eq. (20) is changed to model 3:

$$\sigma_{comp,3} = (1 - p_{pore})^{q/\nu_{Ni}} \sigma_{eff} \tag{21}$$

The q value can be extracted by linearization of Eq. (21):

$$\ln(\sigma_{comp,3}) - \ln(\sigma_{eff}) = \frac{q}{\nu_{Ni}} \ln(1 - p_{pore}) \tag{22}$$

Fig. 7 shows the plots of Eq. (22) with our experimental values for model 3. With this model the different NiO fractions are grouped together. The observation shows that four values lie far outside of this linear approximation (the four points in the dashed circle). The hypothesis is that these values were due to bad electrical contacts. Without these measurements, the R^2 coefficient of the linearization increases from 0.9 to 0.97 and the q value decreases from 1.98 to 1.83. The latter q value is used to fit the experimental measurements in Fig. 8 where the different models are compared.

The simplest model 1 shows much larger values than the measurements. Model 2 with the exponent $k = 3$ gives a reasonable upper bound for the samples containing 60 wt% NiO ($x_1 = +1$). The conductivity measurements of the samples containing 50 and 40 wt% NiO are more dispersed and no value lies close to the upper limit given by model 2. Values for two samples with 40 wt% NiO were equal to zero and not shown in Fig. 8. The conductivity is strongly influenced by the conducting phase fraction (ν_{Ni}), as shown by the mean variation with the NiO content: from 5250 to 2680 and 1130 S cm^{-1} for 60, 50 and 40 wt% NiO, respectively. Model 3, proposed here (Eq. (21)), is incorporating the influence of the volume fraction of conducting phase on the electrical conductivity. A few points lie outside of the model 3 approximation: this can be due again to a contact issue in the measurement method, since it appears for the three different NiO compositions. But it can also come from a percolation issue, as two samples could not be measured at all (sample 10 and 16, see additional on-line support).

The measured samples contain a relatively small nickel fraction if the porosity volume is included, $p_{Ni} = \nu_{Ni}(1 - p_{pore})$, values ranging from 13.9 to 32.4 vol.% Ni. The 13.9 vol.% Ni sample (number 9) showed a conductivity of 170 S cm^{-1} while the non-conductive samples (10 and 16) had a p_{Ni} of 16.1 and 18.1 vol.% Ni, both originally containing 40 wt% NiO. Costamagna et al. showed that the percolation threshold in a two-phase dense packed sphere model depends on the particle size ratio (d_{Ni}/d_{YSZ}) [28]. If the ratio is close to unity, the volume fraction for percolation is 0.294. If the ratio is equal to 0.3 then the percolation should occur around 0.12. Conduction should be possible even for low amounts of nickel if its particles are (much) smaller than YSZ or smaller than the porosity. This model is neither taking into account the high amount of porosity nor the fact that the real particle shapes are different from spheres. But we can consider that porosity is a "non-electronically conductive medium" similar to YSZ. Then sample 9 with $p_{Ni} = 13.5$ vol.% could have had a ratio between nickel particles and YSZ and pore particles smaller than 1/3. It is important to note that the conductivity measurements are done after 24 h under forming gas at 800 °C: it is well known that the nickel phase can sinter under normal SOFC conditions (high temperature and high vapor pressure) [11,12]. After nickel coarsening, the particles ratio between Ni and YSZ will increase and the percolation of the Ni phase could be lost.

4.3. Surface response and model comparison

Comparison of the linear and quadratic models is given in Table 5 using the adjusted coefficient of multiple determination R^2_{adj} (Eq. (5)). In all cases the quadratic model is better, especially for the conductivity and expansion responses. If the addition of parameters between linear and quadratic models did not enhance significantly the fit, the value of R^2_{adj} would have decreased. The model used for the response estimation is thus in all cases quadratic. The regression coefficients of the different responses are given in Table 6. The a_0 estimator is the mean value of the full set of measured samples. For example, the mean value for expansion is 1.39%, a_2 equal to −1.04 means the expansion will decrease by −1.04 when the pore-former weight content changes from $u_2 = 15$–30%, corresponding to $x_2 = 0$ and 1, respectively. When the interaction effect is positive, e.g. a_{14}, the response value will increase if factors 1 and 4 are both positive or both negative. Negative quadratic effects, such as a_{33} and a_{44}, will give a maximum inside the tested region and minimal values at the border as shown by Fig. 9a. The result of high values of a_2 and a_{22} compared to low values of a_1, a_{11} and a_{12}, shows that the response surface for the expansion model depends mainly on the pore-former content (x_2) in Fig. 9b, and hardly on NiO content.

Table 5
Adjusted coefficient of linear regression, R^2_{adj} (Eq. (6)) for linear and quadratic models of the different responses.

R^2_{adj}	Expansion after oxidation (%)	Conductivity (S cm^{-1})	Surface quality	Porosity (%)	Shrinkage (%)
Linear model	0.792	0.748	0.949	0.973	0.995
Quadratic model	0.861	0.879	0.962	0.989	0.996

Table 6
Least square estimates of the quadratic models for the different measured responses.

Estimate	Expansion (%)	Conductivity (S cm^{-1})	Surface quality	Porosity (%)	Shrinkage (%)
a_0	1.39	2124	2.29	30.1	−16.9
a_1	0.10	2455	−0.15	1.8	0.4
a_2	−1.04	−1364	−0.53	9.5	−6.5
a_3	0.30	794	−0.04	−1.9	−0.5
a_4	−0.56	330	−0.32	4.5	3.6
a_{12}	−0.03	−738	−0.01	2.0	0.3
a_{13}	−0.04	1349	0.03	−1.0	−0.1
a_{14}	0.31	−271	0.17	−0.2	−0.4
a_{23}	−0.27	−1553	−0.12	1.9	0.4
a_{24}	0.07	−1034	−0.31	2.6	0.4
a_{34}	0.03	120	−0.05	1.3	−0.1
a_{11}	−0.26	18	−0.11	2.1	1.0
a_{22}	1.53	1090	0.28	−5.7	−1.9
a_{33}	−0.44	258	0.48	−3.0	−0.4
a_{44}	−0.76	−211	−0.61	1.8	0.9

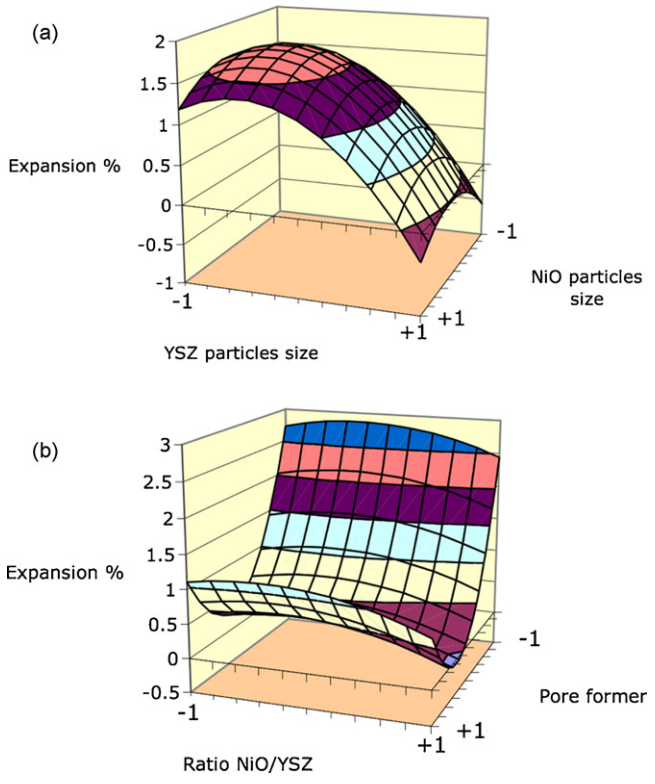

Fig. 9. Expansion surface response model (a) for YSZ and NiO particle size variation with 30 wt% pore-former and 40 wt% NiO and (b) for NiO and pore-former ratio variation for fine NiO and YSZ powders.

A graphical presentation to compare the different relative regression coefficient estimators is given in Fig. 10. 100% corresponds to the value of the constant or mean estimator (a_0).

Increasing the pore-former concentration (a_2) as well as the YSZ particle size (a_4) decreases the expansion (Fig. 10a). This could be related to the porosity response effects (Fig. 10d), the pore-former and the coarse YSZ both increasing porosity. The coarse powder decreases the sinterability, in the opposite way; it increases the porosity [29]. As shown in Fig. 5, porosity and expansion after re-oxidation are correlated. The higher the porosity, the lower the expansion after re-oxidation.

An interesting point is that the NiO content in the composition (a_1 in Fig. 10a) has no influence on expansion; the value of this effect is due to 'noise' as shown by the normal distribution of the coefficients in Fig. 11a. From a_3, coarse NiO seems to be the worst, as it increases expansion. The pore-former has a positive quadratic influence; this is shown by Fig. 9b: for fine YSZ and NiO powders, minimal expansion does not lie at the border of the variables space but at around 15 wt% of pore-former.

The wide range of conductivity values from 16,200 S cm^{-1} (composition 5) to 0 S cm^{-1} (compositions 10 and 16), induces large estimate coefficients of the factors (Fig. 10b). The higher effect is from the NiO content; it is more than 100% of the constant value (a_0). Further, conductivity is decreased by the pore-former content (a_2). The conductivity depends directly on the volume ratio of the metallic phase and the porosity of the sample as seen in the previous section. At high NiO concentration, the effect of NiO particle size is even stronger (from a_{13}). Pore-former content together with high NiO and coarse YSZ particle sizes (a_{23}, a_{24}) lead to a very negative interaction effect on conductivity.

The surface quality decreases by adding pore-former and increasing the YSZ particle size. This is probably due to the lower sinterability with pore-former and coarse YSZ, to yield damaged sample surfaces. If both factors are increased, the effect on surface quality is even worse due to the negative interaction estimator (a_{24}) in Fig. 10c. The quadratic effects are important for surface quality compared to the main effects: a positive quadratic effect gives maxima at the borders of the studied region for pore-former and NiO particle size. For the YSZ particle size it is at the center of the domain that the maximal surface quality can be found.

In summary, the major effect is given by the pore-former addition, which increases the as-sintered porosity and reduces the expansion on re-oxidation. The coarse YSZ particles give a similar response due to lower sinterability. The NiO content only affects

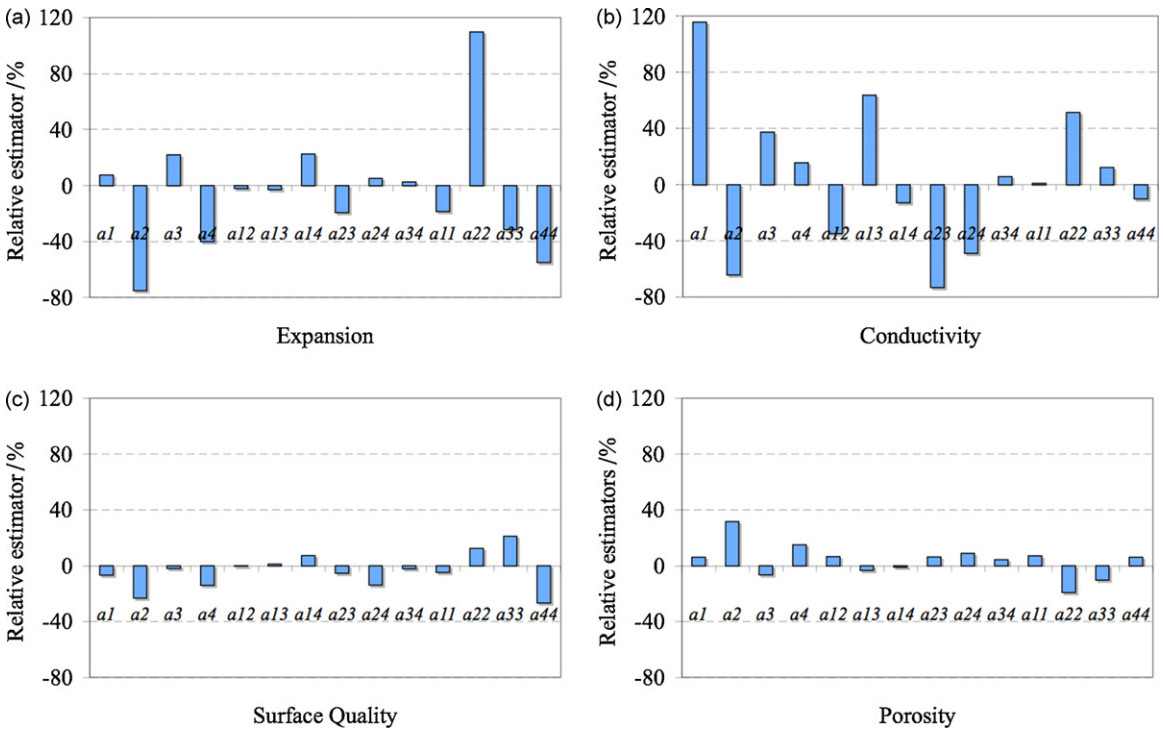

Fig. 10. Relative regression estimator coefficient (half-effect) of the quadratic model for (a) expansion after one RedOx cycle at 845 °C, (b) conductivity at room temperature after 24 h of reduction, (c) surface quality after sintering and (d) porosity after sintering. All half-effects are divided by their constant effect a_0.

the conductivity, with no threshold value observed. The NiO particle size does not show any significant effect on the studied response (the estimator coefficient, a_3, is not significant), which could be due here to the fact that coarse NiO was made from agglomerates broken down during the ball-milling process.

4.4. Optimized compositions

The optimal composition should present a correct surface quality (SQ response) after sintering in order to produce SOFC half-cells, with dense thin electrolyte e.g. for subsequent cathode screen-

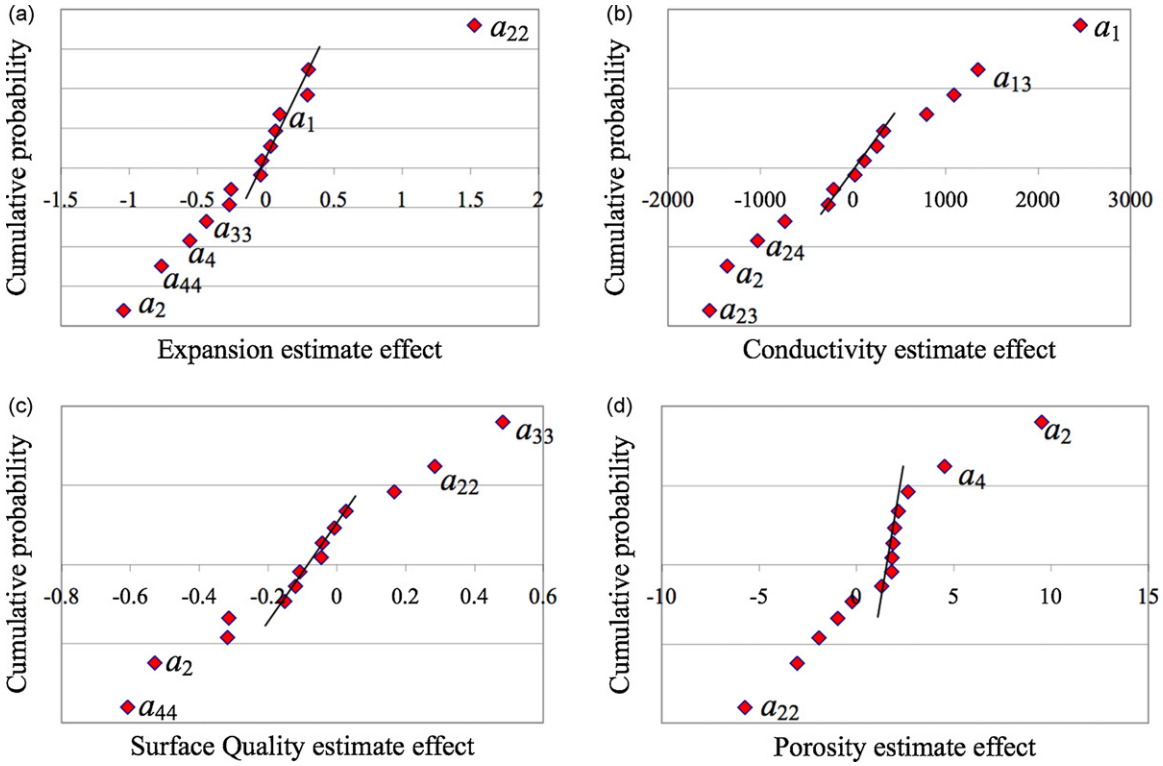

Fig. 11. Regression estimator coefficient (half-effect) normal plot for (a) expansion after one RedOx cycle at 845 °C, (b) conductivity at room temperature after 24 h of reduction, (c) surface quality after sintering and (d) porosity after sintering.

Table 7
Optimized compositions fulfilling the requirements. Surface quality ≥ 1.65, conductivity at room temperature ≥ 500 S cm^{-1} and expansion ≤ 0.2%.

Case	Compositions				Response of the models		
	NiO ratio (wt%)	Pore-former (wt%)	NiO particle size	YSZ particle size	Expansion (%)	Conductivity (S cm^{-1})	Surface quality
1	40	3	Fine	Coarse	0.10	1554	2.60
2	40	10	95% Coarse	Coarse	−0.29	518	1.66
3	40	20	Fine	Coarse	−1.48	837	1.65
4	50	7.5	95% Fine	Coarse	0.16	2402	2.28
5	50	15	Fine	Coarse	−0.70	1587	1.94
6	60	9	Fine	Coarse	0.03	3247	2.16
7	60	15	Fine	Coarse	−0.50	2440	1.82
8	60	20	Fine	Fine	−0.07	2807	2.03

printing and stack assembling. It also should possess sufficient conductivity and show an expansion after re-oxidation lower than 0.2%. The limitation of electrical conductivity is given by the thickness of the anode support and the distance between the electrical contacts at the surface of the anode. Conductivity at 800 °C higher than 100 S cm^{-1} is an adequate target. The variation of electrical conductivity of the cermet with temperature has been measured by Wei and Atkinson [30]. The electrical conductivity at 800 °C is about 20% of the value at room temperature. Hence a limit of 500 S cm^{-1} measured on the sample at room temperature can be suggested as criterion (Table 7).

To find an optimum composition, the lowest surface quality (SQ) limit is arbitrarily fixed at 1.65, the lowest (room temperature) conductivity value at 500 S cm^{-1} and the highest expansion limit after re-oxidation at 0.2%. The compositions that fulfill these conditions are presented in four 3D graphs with the axes corresponding to the different factors. From Fig. 12, it is possible to find different compositions that are in agreement with these requirements. Negative values of expansion are due to the quadratic model fit. It is interesting to note that appropriate compositions can be found over the full range of studied NiO content (40–60 wt% NiO) and YSZ powder size. The pore-former content can vary from 3 to 20 wt% and the

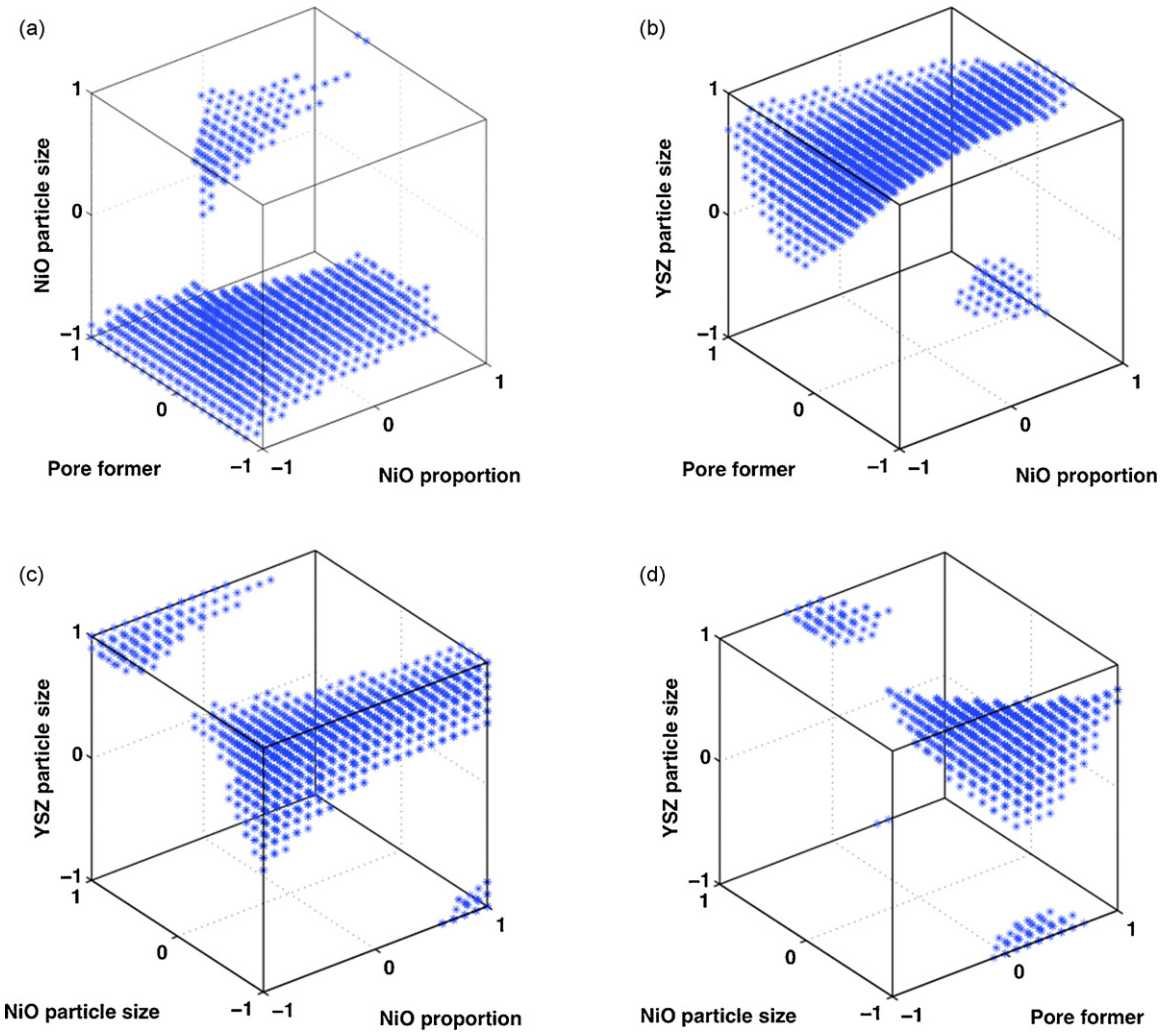

Fig. 12. Compositions where surface quality ≥ 1.65, conductivity ≥ 500 S cm^{-1} and expansion ≤ 0.2%.

NiO powder size from 5 to 100% fine fraction. These compositions will in future be tested as anode supports for SOFC.

5. Conclusion

A design of experiment approach was efficiently applied to the microstructure optimization of the Ni/YSZ anode support for RedOx stability enhancement. Quadratic models give a significantly better experimental fit than linear models.

The major advantage of this work compared to previous studies is the wide domain of experimental space (81 possible compositional combinations) covered with a reduced number of experiments (25 variance-optimized compositions and 46 tested samples), with a method giving the statistics to extract individual and combined effects of the different experimental variables on the study's final target, i.e. the limited re-oxidation strain of the Ni–YSZ anode support.

The RedOx-safe expansion limit lower than 0.2% is reached only for samples with as-sintered porosity at least higher than 35%, and rather around 50%, for the parameter space covered in this study. The major factors lowering the expansion are correlated to the ones increasing porosity: pore-former fraction and YSZ powder size. Coarse zirconia powder has lower sinterability and so increases final sample porosity.

Conductivity is influenced principally by the NiO content and secondly by the as-sintered porosity.

As a result of the approach, eight compositions reaching expansion smaller than 0.2%, conductivity higher than 500 S cm^{-1} and good sample surface quality are defined. Forthcoming work will consist in selecting several of these compositions to be produced by tape casting and electrochemically tested.

Acknowledgments

Kind acknowledgements are extended to HTceramix® SA (Switzerland) and SOFCpower® (Italy) for the materials supply, to the Powder Technology Laboratory in EPFL (Prof. H. Hofmann and C. Morais) for TGA analysis facilities, to the Ceramic Laboratory (Prof. N. Setter and J. Castano) for the furnace and cell fabrication facilities and to the European Institute for Energy Research (EIfER, Karlsruhe, Germany) for the financial support (contract no N43/C06/019).

Appendix A. Supplementary data

Supplementary data associated with this article can be found, in the online version, at doi:10.1016/j.jpowsour.2010.07.092.

Appendix B

Here the derivation is given to calculate the different fractions (weight, volume and molar) in a composite (w: weight fraction, ν: volume fraction in the solid phase, n: mole fraction, p_i: volume fraction including porosity) [2,31]. The composite is based on phase 1 and 2. When the subscript is not written, the fraction is for component 1. In the case of Ni/NiO–YSZ composite the subscripts are 1, *red* for Ni, 1,*ox* for NiO, 2 for YSZ, and *pore* for porosity. The density is ρ, the molar volume, V and the molar mass, M. The sample volume is considered as constant during the state change (from oxidized to reduced state).

Density of the composite:

$$\rho_{th} = \frac{\rho_1 \rho_2}{w\rho_2 + (1-w)\rho_1} \tag{B1}$$

Table B1
Density, molar mass and molar volume of the components of the studied composite.

	Ni	NiO	8YSZ
ρ/(g cm^{-3})	8.89	6.67	5.90
M/(g mol^{-1})	58.71	74.71	127.87
V/(cm^3 mol^{-1})	6.604	11.20	21.67

Weight to molar:

$$n = \frac{wM_2}{wM_2 + (1-w)M_1} \tag{B2}$$

Molar to weight:

$$w = \frac{nM_1}{nM_1 + (1-n)M_2} \tag{B3}$$

Weight to volume:

$$\nu = \frac{w\rho_2}{w\rho_2 + (1-w)\rho_1} \tag{B4}$$

Volume to weight:

$$w = \frac{\nu\rho_1}{\nu\rho_1 + (1-\nu)\rho_2} \tag{B5}$$

Volume to molar:

$$n = \frac{\nu V_2}{\nu V_2 + (1-\nu)V_1} \tag{B6}$$

Molar to volume:

$$\nu = \frac{nV_1}{nV_1 + (1-n)V_2} \tag{B7}$$

Volume oxidized to volume reduced:

$$\nu_{red} = \frac{\nu_{ox} V_{1,red}}{\nu_{ox} V_{1,red} + (1-\nu_{ox})V_{1,ox}} \tag{B8}$$

Weight oxidized to weight reduced:

$$w_{red} = \frac{w_{ox} M_{1,red}}{w_{ox} M_{1,red} + (1-w_{ox})M_{1,ox}} \tag{B9}$$

Including porosity fraction in oxidized state (same for the reduced state):

$$p_{1,ox} + p_{2,ox} + p_{pore,ox} = 1$$

$$\frac{p_{1,ox}}{\nu_{1,ox}} = \frac{p_{2,ox}}{\nu_{2,ox}} = 1 - p_{pore,ox} \tag{B10}$$

Porosity after reduction (for a constant sample volume):

$$p_{pore,red} = -\Delta V_{red} \nu_{1,ox}(1 - p_{pore,ox}) + p_{pore,ox} \tag{B11}$$

$$\text{with } \Delta V_{red} = \frac{V_{1,red}}{V_{1,ox}} - 1 \tag{B12}$$

References

[1] S.C. Singhal, K. Kendall, High Temperature Solid Oxide Fuel Cell–Fundamentals, Design and Applications, Elsevier, Oxford, 2003.
[2] A. Faes, A. Nakajo, A. Hessler-Wyser, D. Dubois, S. Modena, A. Brisse, J. Van herle, J. Power Sources 193 (2009) 55–64.
[3] T. Klemensoe, Topsoe Fuel Cell, Technical University of Danemark, Risoe National Laboratory, 2005.
[4] D. Sarantaridis, A. Atkinson, in: U. Bossel (Ed.), Proceedings of the 7th European Solid Oxide Fuel Cell Forum, Lucerne, Switzerland, 2006, p. P0728.
[5] Z. Wuillemin, N. Autissier, M. Nakajo, M. Luong, J. Van herle, D. Favrat, J. Fuel Cell Sci. Technol. 5 (2008) 0110161–0110169.
[6] D. Waldbillig, A. Wood, D.G. Ivey, Solid State Ionics 176 (2005) 847–859.
[7] M. Pihlatie, T. Ramos, A. Kaiser, J. Power Sources 193 (2009) 322–330.
[8] S.P. Jiang, S.H. Chan, J. Mater. Sci. 39 (2004) 4405–4439.
[9] D.W. Dees, T.D. Claar, T.E. Easler, D.C. Fee, F.C. Mrazek, J. Electrochem. Soc. 134 (1987) 2141–2146.
[10] J.H. Lee, H. Moon, H.W. Lee, J. Kim, J.D. Kim, K.H. Yoon, Solid State Ionics 148 (2002) 15–26.

[11] D. Simwonis, F. Tietz, D. Stoever, Solid State Ionics 132 (2000) 241–251.
[12] A. Faes, A. Hessler-Wyser, D. Presvytes, C.G. Vayenas, J. Van herle, Fuel cells 9 (2009) 841–851.
[13] R.A. Fischer, Statistical Methods for Research Workers, Oliver and Boyd, Edinburg and London, 1925.
[14] R.A. Fischer, The Design of Experiment, Oliver and Boyd, Edinburg and London, 1935.
[15] G.E.P. Box, J.S. Hunter, W.G. Hunter, Statistics for Experimenters—Design, Innovation and Discovery, 2nd ed., John Wiley & Sons, Hoboken, 2005.
[16] R.H. Myers, C.M. Montgomery, C.M. Anderson-Cook, Response Surface Methodology—Process and Product Optimization using Designed Experiments, 3rd ed., John Wiley & Sons, Hoboken, 2009.
[17] Y. Wang, T.W. Coyle, J. Therm. Spray Technol. 17 (2008) 692–699.
[18] G. Rajaram, S. Desai, Z. Xu, D.M. Pai, J. Sankar, Int. J. Manuf. Res. 3 (2008) 350–359.
[19] B. Wahdame, D. Candusso, X. Francois, F. Harel, M.C. Pera, D. Hissel, J.M. Kauffmann, IEEE Trans. Energy Convers. 23 (2008) 1093–1104.
[20] CRC Handbook of Chemistry and Physics, 53rd ed., CRC Press, Cleveland, 1973.
[21] J.E. Cleland, J.W. Evans, E.E. Fauser, W.R. Fetzer, Ind. Eng. Chem. Res. 16 (1944) 161–165.
[22] J. Van herle, R. Ihringer, R. Vasquez Cavieres, L. Constantin, O. Bucheli, J. Eur. Ceram. Soc. 21 (2001) 1855–1859.
[23] D. Simwonis, H. Thuelen, F.J. Dias, A. Naoumidis, D. Stoever, J. Mater. Process. Technol. 92–93 (1999) 107–111.
[24] P. Bowen, J. Dispers. Sci. Technol. 23 (2002) 631–662.
[25] M. Radovic, E. Lara-Curzio, Acta Mater. 52 (2004) 5747–5756.
[26] R.M.C. Clemmer, S.F. Corbin, Solid State Ionics 180 (2009) 721–730.
[27] C.E. Baumgartner, R.H. Arendt, C.D. Iacovangelo, B.R. Karas, J. Electrochem. Soc. 131 (1984) 2217–2221.
[28] P. Costamagna, P. Costa, V. Antonucci, Electrochim. Acta 43 (1998) 375–394.
[29] H. Luebbe, J. Van herle, H. Hofmann, P. Bowen, U. Aschauer, A. Schuler, F. Snijkers, H.J. Schindler, U. Vogt, C. Lalanne, Solid State Ionics 180 (2009) 805–811.
[30] X. Wei, A. Atkinson, J. Electrochem. Soc. 152 (2005) C513–C519.
[31] A. Muller, PhD Thesis, Fakultät für Elektotechnik und Informationstechnik, Universität Fridericiana zu Karlsruhe genehmigte, Karlsrhue, Germany, 2004.